

Gaze-based Object Detection in the Wild

Daniel Weber*[†]

University of Tübingen

daniel.weber@uni-tuebingen.de

Wolfgang Fuhl*

University of Tübingen

wolfgang.fuhl@uni-tuebingen.de

Andreas Zell

University of Tübingen

andreas.zell@uni-tuebingen.de

Enkelejda Kasneci

Technical University of Munich

enkelejda.kasneci@tum.de

January 26, 2023

Abstract

In human-robot collaboration, one challenging task is to teach a robot new yet unknown objects enabling it to interact with them. Thereby, gaze can contain valuable information. We investigate if it is possible to detect objects (object or no object) merely from gaze data and determine their bounding box parameters. For this purpose, we explore different sizes of temporal windows, which serve as a basis for the computation of heatmaps, i.e., the spatial distribution of the gaze data. Additionally, we analyze different grid sizes of these heatmaps, and demonstrate the functionality in a proof of concept using different machine learning techniques. Our method is characterized by its speed and resource efficiency compared to conventional object detectors. In order to generate the required data, we conducted a study with five subjects who could move freely and thus, turn towards arbitrary objects. This way, we chose a scenario for our data collection that is as realistic as possible. Since the subjects move while facing objects, the heatmaps also contain gaze data trajectories, complicating the detection and parameter regression. We make our data set publicly available to the research community for download.

1 Introduction

Recent research has shown that eye tracking has becoming increasingly relevant for a variety of applications. These include even dynamic real-world scenarios, such as driving [22], [2], [39], medicine [35], [9], [33], and sports [8], [11], [24]. Especially the combination with computer vision problems [34], [29], has in turn great potential for the employment of eye tracking in other fields, such as robotics [23],[3], [37]. In the field of robotics, the focus is often on the interaction with the environment, for example, detecting and grasping objects [14], [21]. In such settings, however, the interaction entities are often unknown due to the enormous amount of potentially existing objects. For this purpose, a semantic understanding of scenes must be present. In conveying this understanding, humans can play an important role and provide assistance to the robot. One modality that has proven to be particularly suitable and helpful for such human-robot collaboration settings is the human gaze [36]. Gaze allows objects to be intuitively selected by the human and communicated (e.g., gaze pointing) to the interaction partner (e.g., robot). An additional advantage of the gaze modality is that it is far more unambiguous than gestures and, unlike speech, can also be used effortlessly in the case of unknown objects whose class name may not be known at all.

In this work, we address the problem of unknown object detection in real-world scenarios based on gaze. This is an essential challenge for human-robot collaboration, as an example. After all, if the robot could detect an unknown object by the fact that the human is looking at it, this paves the way for further interaction possibilities. We refer to object detection in a similar manner to face detection. In face detection, the task is to estimate whether there is a face or not. In our task, the challenge is to

*Both authors contributed equally to this research.

[†]Funded by the Deutsche Forschungsgemeinschaft (DFG, German Research Foundation) under Germany's Excellence Strategy – EXC number 2064/1 – Project number 390727645.

find out whether the current gaze pattern belongs to a perceived object or not. While there is work investigating unknown object detection on static imagery, there is little research addressing unknown object detection on videos and settings in the wild. Along this line, [16] and [38] used fixations to infer the saliency of objects. A gaze map was used by [30], who combined it with candidate regions to segment objects. In addition, the authors in [40] investigated the relationship between fixations made while observing an image and the object categories it contains. The finding was that machine learning models can benefit from human fixations for detection and classification tasks. In the work by [20], gaze points were grouped into clusters to determine whether a cluster belonged to an object of interest and whether it was looked at intentionally or unintentionally. However, all these related works used multiple gaze points on one image, which is only possible if the stimulus (image of the observed scene) is static or if, for instance, eye tracking data from multiple people is used, as in [29]. In the latter, it was possible to extract attentionally important objects from videos. Contrary to all aforementioned related works, we present a method capable of using gaze data from a single person in dynamic scenes, i.e., with non-static stimuli, to detect unknown objects.

Our way to meet this challenge is by considering and analyzing gaze data across multiple frames and constructing a heatmap from it. In contrast, [37] significantly reduced the amount of candidate bounding boxes of unknown objects on a static image using only one gaze point. In another recent work in a human-robot collaboration scenario, [36] achieved segmentation of unknown objects and calculated corresponding bounding boxes in 3D space in real time. Although only one gaze point was required here, the scene image including depth information was needed. Some other approaches dispense with the gaze altogether, but focus rather on single-class images [25], [15], or use additional information, e.g., from a depth sensor [1]. While robots typically have many sensors, they often have limited computing power and, in some cases, not even a graphics processor, so using large amounts of image data, especially depth images, puts a lot of strain on them. Additionally, there is often only one object of interest at a time, obviating the need to detect all objects at once. By completely omitting image data and employing gaze data instead, we can accomplish the task of detecting unknown objects of interest and still saving large amounts of required computer resources.

In this work, we build on existing work and pave the way for successful human-robot interaction through the following main contributions:

- We present a method for detecting unknown objects in a scene without stimulus, based solely on gaze information.
- We only use heatmaps instead of scene images, enabling thus for a significantly faster approach than image-based object detection, while at the same time requiring considerably less computational resources.
- In a proof of concept, we evaluate the accuracy of different machine learning techniques and parameters, such as the time window size for the spatial distribution of the gaze data and the grid size of the resulting heatmaps.
- We make our unique data set, which contains both gaze data and bounding boxes of the observed objects, publicly available to the research community for download at <https://cloud.cs.uni-tuebingen.de/index.php/s/QPzJC48xDGsJnZK>.

2 Method

In this work, we challenge object detection by means of gaze points. Here we follow two goals. First, we classify which gaze points or ranges of gaze points belong to an object, and we assign temporal windows to the gaze points, which belong to an annotated bounding box. This creates a classification problem in which the gaze points windows with an associated bounding box are assigned to class one and gaze points windows without a bounding box are assigned to class zero.

The second goal is to regress the bounding box parameters on the gaze points. These parameters are the width and height, as well as the x and y position. For this task, we also assigned the gaze points to temporal windows. For the regression, we used only temporal windows with associated bounding box, since all other temporal windows have no parameters for the regression.

We decided to use a spatial distribution as a feature since this worked best in our initial evaluations. This spatial distribution is a heatmap as previously proposed by [6] to classify gaze position data. To

create such a heatmap, the gaze position data of a temporal window are used, and the individual gaze positions are assigned to cells in the heatmap (grid). Each time window results in one heatmap. The assignment procedure is illustrated in Fig. 1. After the assignment, the heatmap is divided by the sum

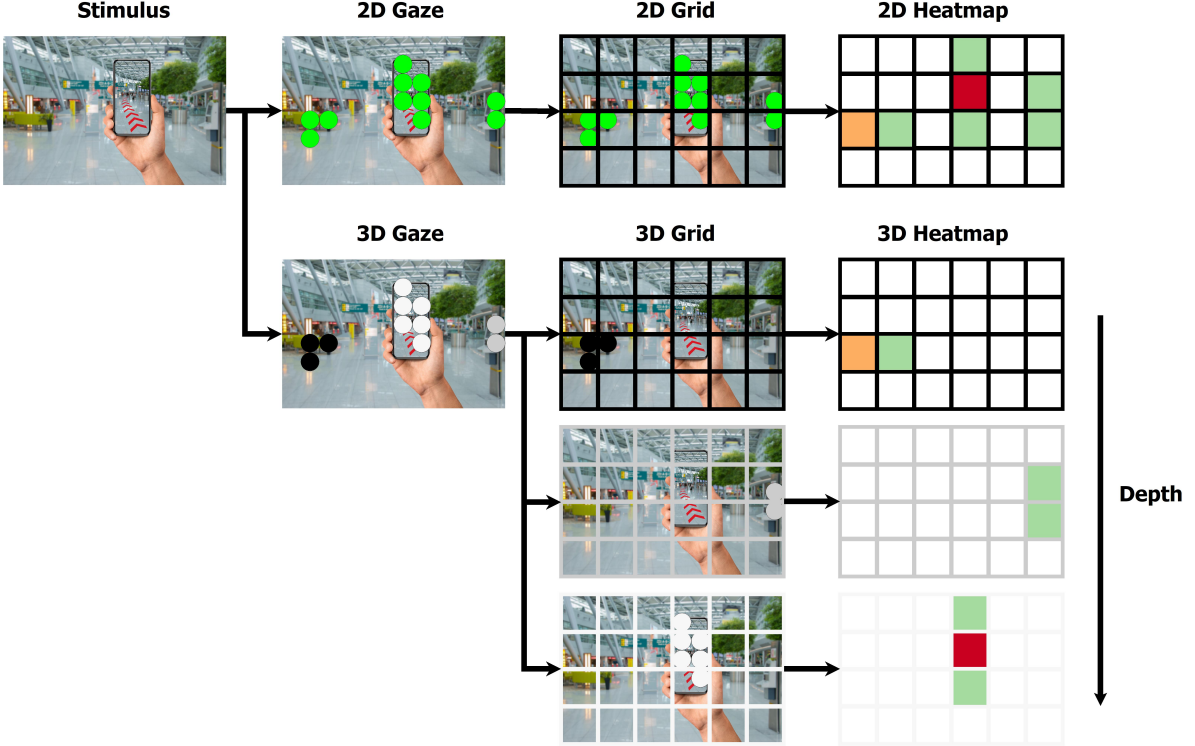


Figure 1: Creation of a 2D or 3D heatmap based on the gaze information and the stimulus resolution.

over all values to obtain a distribution. As an extension to the approach in [6], we extended the 2D heatmap to 3D. This was possible because the software used for gaze determination generates 3D gaze points [7] based on a k -nearest neighbor regression. In the case of the 3D heatmap, a cell is assigned to each gaze point based on its spatial position with the difference to the 2D heatmap that the depth or distance of the gaze points is additionally considered along the z -axis. An example of an assignment of gaze points to a 3D heatmap can be seen in Fig. 1.

A formal description of the generation of the heatmap in 3D is given in Equation 1.

$$\text{heat} \left(\left\lfloor \frac{p_x}{R_x} \cdot G_x \right\rfloor, \left\lfloor \frac{p_y}{R_y} \cdot G_y \right\rfloor, \left\lfloor \frac{p_z}{R_z} \cdot G_z \right\rfloor \right) += 1. \quad (1)$$

The gaze positions in x , y , and z coordinates in an Euclidean coordinate system are denoted by p_x , p_y , and p_z , respectively. The constants R_x , R_y , and R_z represent the maximum resolution of the stimulus in x and y direction and the maximum depth supported by the software Pistol [7]. By dividing the gaze points by the maximum resolution, these ranges are normalized between 0 and 1. Subsequently, these values are multiplied by the number of grid cells (G_x , G_y , and G_z) and rounded to the nearest integers, denoted by “ $\lfloor \cdot \rfloor$ ”. These new values correspond to the index in the heatmap and the selected cell is incremented by one, denoted by “ $+=$ ”. In the case of a 2D heatmap, the cell for depth (z coordinate) is fixed at one.

Equation 2 describes the normalization of the heatmap in 3D and 2D since for the 2D case there would be only one depth.

$$\text{heat}(x, y, z) = \frac{\text{heat}(x, y, z)}{\sum_{i=1}^{G_x} \sum_{j=1}^{G_y} \sum_{k=1}^{G_z} \text{heat}(i, j, k)}. \quad (2)$$

Our normalization sums up the entire heatmap and divides each value of the heatmap by this sum. The variables x , y , and z are the indexes to the heatmap corresponding to the x -axis, y -axis, and z -axis.

As in Equation 1, the variables G_x , G_y , and G_z are the maximum amount of grid cells in the heatmap. Finally, the one-dimensional vector resulting from the flattening of the heat map can be used as an input feature for various machine learning techniques.

3 Study Design & Data Acquisition

In this section, we describe the dataset we used. In order to evaluate our approach, a dataset was required which contains not only eye tracking information but also, in addition to the gaze points, the bounding boxes of the objects that the participants were looking at. Since, to the best of our knowledge, no such dataset exists or is publicly available, we collected a novel data set. In the beginning, we gave each of the five subjects an introduction to the recording procedure. Each recording started with a calibration. To this end, the participants were instructed to stand 0.5 m in front of the calibration marker and look at its center. They were then asked to walk backward for about five meters, slowly circling their head while fixating on the center of the marker throughout. Subsequently, the subjects were allowed to move freely around the site, both inside and outside the building, a university complex with several floors, corridors, and offices on the inside and a street, parking lots, and green areas on the outside. In this course, they should look at arbitrary objects they encountered, such as first aid kits, fire extinguishers, light switches, door signs, street signs, trees, and bicycles, among others. There was no specification as to how long they were supposed to look at the objects. To evaluate gaze accuracy, the participants were asked to look at the calibration marker again at the end of each recording. Initially, five meters away, they had to move towards the marker with head rotations until they were standing directly in front of it. Due to the different distances, we are able to estimate depth information in both calibration and evaluation data via the tool Pistol [7]. All recordings were conducted with the Pupil Invisible eye tracker, a head-mounted eye tracker developed by Pupil Labs [26], whose scene camera provides RGB images with a resolution of 1088×1080 . Each participant captured three recordings (each recording was about five minutes long, including calibration and evaluation), resulting in 15 videos in total. Only one recording could not be used due to an incorrectly performed calibration, where the marker was in the image of the scene for a while without the subject looking at it. Even though the tool Pistol filters out a certain amount of erroneous data, the incorrect portion was too large during the calibration phase. This led to a total length of about one hour of recording, consisting of 102 620 frames of which 27 946 contained objects.

Finally, we labeled the obtained data with DarkLabel [4]. The objects in the dataset, respectively their bounding boxes, have the characteristics shown in Table 1.

Table 1: Size distribution of the objects in the dataset. The numbers indicate the size of the respective bounding box in pixels. Note that the columns do not have to originate from the same bounding box. The mean is denoted by μ and the standard deviation by σ .

	Width	Height	Size
min	16	18	288
max	1056	955	830 484
μ	177	227	61 456
σ	154	185	103 384

Fig. 2 shows individual example moments from the recordings. Due to the errors related to the gaze estimation, the gaze points are not always on the labeled object, even though the participant was actually looking at it. In fact, even for a human, it is not always easy to determine the target object, and sometimes only possible considering the context and the observation of an image sequence. This demonstrates quite clearly the difficulties and challenges associated with this task. Our final, publicly available dataset only contains the gaze information and bounding boxes, yet no stimuli-related information.

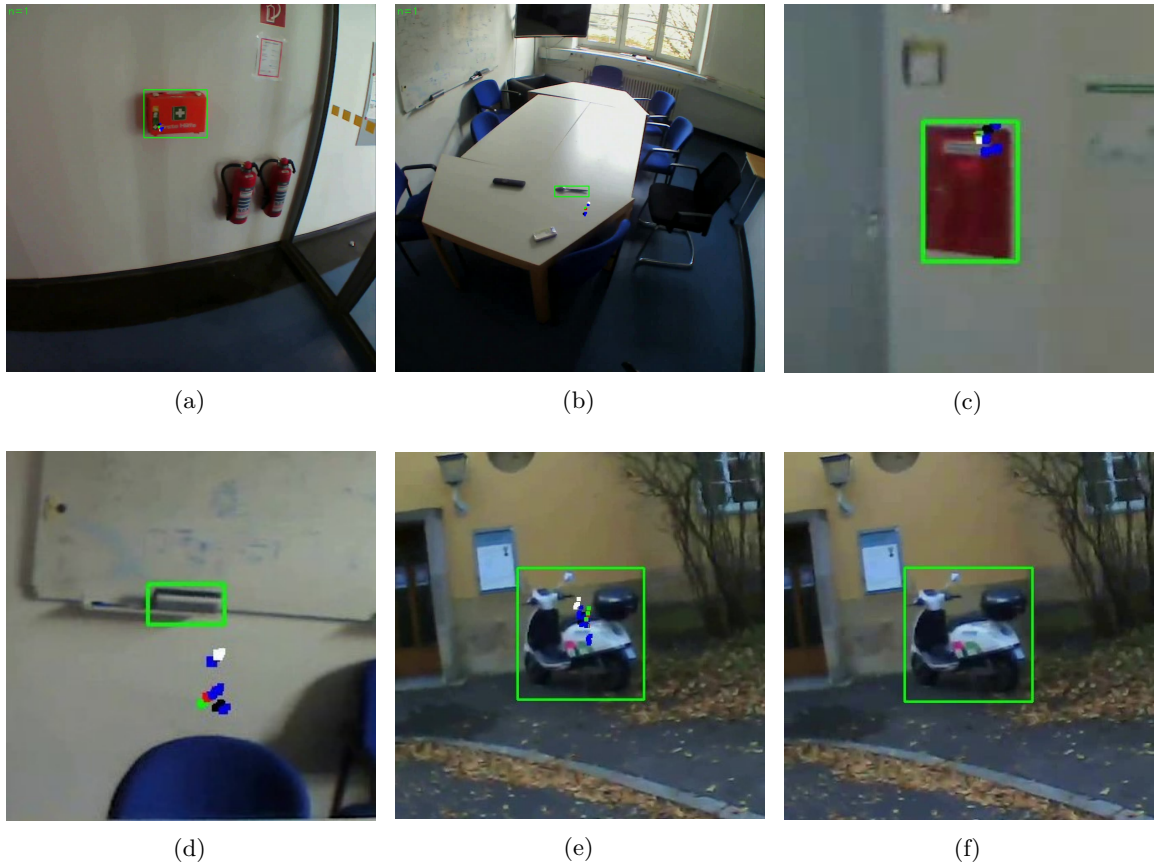


Figure 2: The images show exemplary moments of our data, where the objects that were consciously observed are labeled with a bounding box. The first two images (a) and (b) show the entire field of view of the scene camera (1088×1080), while the other images (c)–(f) have been zoomed in to better show the bounding box and the various estimated gaze points. The gaze points are colored depending on the estimation method used by Pistol [7]. In (b) and (d), the gaze points do not lie within the bounding boxes since the gaze estimation is — especially for smaller objects — not always completely accurate. As in the last image (f), there may also be occasionally no gaze points in between. In light of these challenges, gaze-based object detection is a non-trivial problem.

4 Evaluation

In this section, we evaluate the classification of the gaze points with respect to the affiliation to an object, and we try to extract the position and the size of the object from those. To this end, we applied a variety of different, well-established machine learning methods and list here a selection comprising the best of them. For easy reproducibility of our approach, we restrict ourselves to Matlab’s standard parameters of the used machine learning methods. In the classification experiments, we always specify the mean accuracy of a 5-fold cross validation. For the regression experiments, the mean error as a percentage of the image resolution from a 5-fold cross validation is given. We evaluated different heatmap grid sizes as well as different time window sizes. Furthermore, we investigate the runtime and memory requirements of our method and compare it to state-of-the-art object detectors. We conducted our evaluations on a computer system with Windows 10 as the operating system, an AMD Ryzen 9 3950X 16-core processor with 3.50 GHz, and 64 GB DDR4 Ram. All machine learning methods were implemented on the Matlab version 2021b.

The assignment of classes (object or no object) to time windows was done based on the presence of an annotated object in the time window. This means that if there was an annotated object in the time window, the class was set to one. If this was not the case and there was no annotated object in the time window, the class was assigned zero. In the regression, only time windows with an existing annotated object were used. Here, the parameters of the annotated object closest to the central timestamp of

the time window were chosen. This was assigned because, in most cases, our subjects moved while looking at an object. Thus, there are usually different positions and sizes of bounding boxes in a time window. To compensate for this, the most central object in time was always chosen. The conversion of the time windows into seconds can be roughly calculated using the formula $\text{Sec} = T / (6.66 \cdot 30)$, where T is the size of the respective time window in frames (eye camera). This is due to the recording rates of the scene camera (30 frames per second) and the recording rate of the eye camera (200 frames per second) of the Pupil Invisible [26] eye tracker. The 6.66 is the number of eye frames per scene image. An alternative formulation is to divide the time window size T by the number of eye frames per second, which is 200.

Fig. 3 and Table 2 show the results of our classification experiment. Comparing the results of the

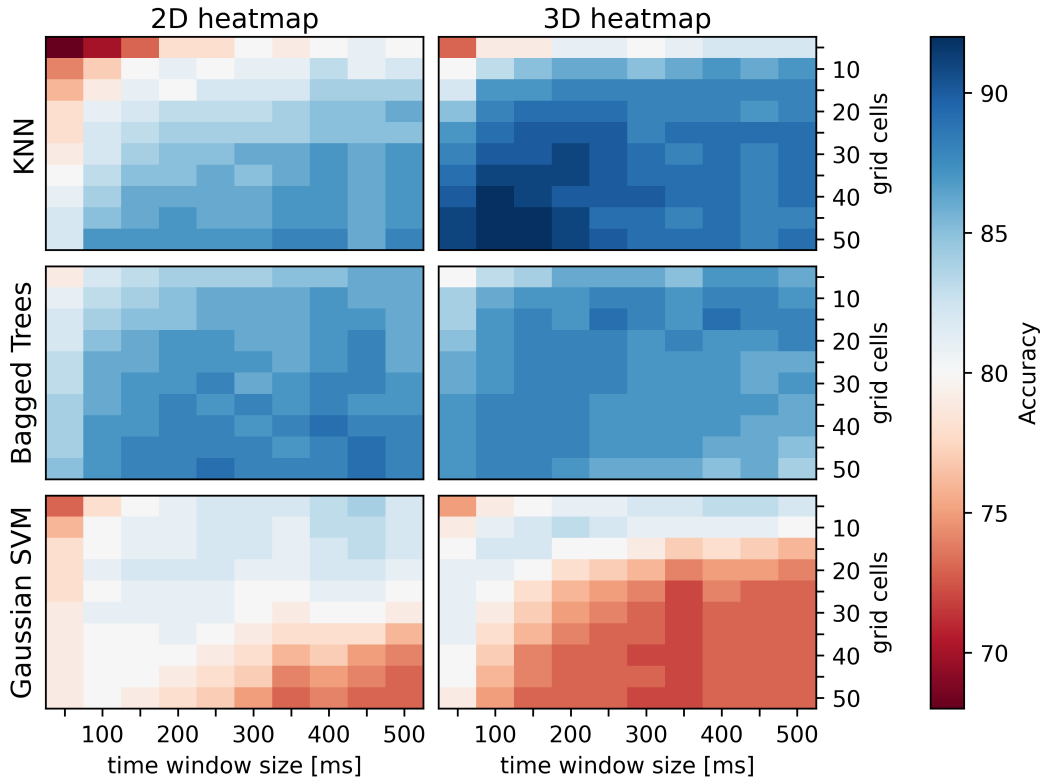


Figure 3: Classification results of the 2D and 3D heatmap features for different time window sizes (in ms), number of grid cells, and machine learning methods illustrated in a heatmap. The results are the average accuracy of a 5-fold cross validation.

Table 2: Best and worst classification results of the 2D and 3D heatmap features. The mean is denoted by μ and the standard deviation by σ .

Feature	ML	Accuracy		
		Worst	Best	$\mu \pm \sigma$
2D heatmap	KNN	68	88	83.2 ± 3.8
	Bagged Trees	79	89	86.3 ± 1.9
	Gaussian SVM	73	84	79.4 ± 2.6
3D heatmap	KNN	73	92	87.8 ± 3.3
	Bagged Trees	80	89	86.8 ± 1.3
	Gaussian SVM	72	83	76.5 ± 3.6

three methods, i.e., KNN, bagged trees, and Gaussian SVM, it can be seen that for the 2D heatmap feature, the approach based on bagged trees achieves the best results. Looking at the progression over

the grid size and the time window size, we can see that the KNN and the bagged trees perform best with a high number of grid cells and large time windows. In the case of the Gaussian SVM, this is different, as this method performs best at a small number of grid cells but still large time windows. Moving on to the 3D heatmaps, the accuracy of the KNN method improves by 4 percent to 92 percent, which is also significantly better than the bagged trees. The bagged trees do not improve overall and remain at 89 percent.

The results of our regression experiment are shown in Table 3. To calculate a reasonable pixel value from the results, one must multiply them by ten. This is because the results are entered relative to the screen resolution (values between zero and one) and the mean absolute error was multiplied by 100 to obtain the percentage. Since the scene resolution is approximately 1000×1000 pixels, multiplying by ten is sufficient. Looking at the individual methods (Gaussian process regression, bagged trees, and Gaussian SVM), we see that all methods perform similarly well. As expected, based on the spatial heatmap feature, the position estimation is the most accurate. In contrast, the regression of the bounding box size, using only gaze data and no stimuli, is even more difficult than the position estimation and therefore less accurate. Comparing the results for the 2D and the 3D heatmap feature, the position results remain about the same, with some overall improvement. In terms of bounding box size, the best results improve significantly for all of the three methods. All in all, the Gaussian process method combined with the 3D heatmap feature performs best.

Fig. 4 shows a small part of the results of the Gaussian process regression in comparison to the ground truth. As can be seen, the determination of the X and Y position is quite accurate, whereas there are some outliers in the determination of the bounding box size. This is mainly due to the fact that in many cases the entire object was annotated, but not the whole object was observed. For this reason, the actual size cannot be estimated from the gaze data in these cases. Nevertheless, this is the way humans naturally look at objects in their environment, and it can be seen from the plots of the width and height of the bounding box that the method still works very well overall.

In the following, we will compare our approach with a baseline to better classify its performance. It should be borne in mind that classical object detectors, such as FCOS [32] or Faster R-CNN [27], pursue a slightly different goal than we do. Whereas in their case all objects are usually to be detected, we are primarily interested in the existence of an object of interest, that is, the one that the human is looking at. Since classical object detectors only use images of the scene and do not obtain information about human gaze behavior, they cannot know whether a human has looked at an object and, if so, which object. Thus it would be basically a matter of chance whether the statement that a person looks at an object is true or false.

With the regression task, the detection of all objects would be possible. Here, however, we encounter a different real-world problem, outside of laboratory conditions, which also makes our method so appealing. Since we are in a wild world, the objects of interest are extremely diverse and their number tremendous. The vast majority of objects in our dataset, such as doorknobs, light switches, and fire extinguishers, are simply not part of any publicly available data sets, such as Microsoft COCO [18] or ImageNet [5], that are typically used for training. Since the methods differ too much in this respect, we need a benchmark that covers more the commonalities. Therefore, in the remainder of this section, we will establish a baseline comparison in terms of speed and computing resources. As a baseline, we use state-of-the-art object detectors. These include Faster R-CNN [27], FCOS [32], and RetinaNet [17], each with a ResNet-50-FPN backbone [10], SSDlite320 [19] and Faster R-CNN both with a MobileNetV3 Large backbone [28, 12], as well as SSD300 [19] with a VGG16 backbone [31]. These are supplemented by the YOLOv5 [13] variants YOLOv5n, YOLOv5s, YOLOv5m, YOLOv5l and YOLOv5x. All of these object detectors were trained on Microsoft COCO and all backbones were trained on ImageNet. In order to test the speed, we measured the runtime of all methods on the CPU for 1000 individual predictions, i.e. 1000 different inputs with a batch size of 1. The resource consumption was determined by measuring the amount of memory required for a single input. For our method with the heatmap input features, we used a time window size of 250 ms. For the classic object detectors, the $1088 \times 1080 \times 3$ RGB images were used as input. The results are shown in Table 4.

The fastest is the Gaussian SVM with the 2D heatmap feature and a grid cell number of 10, taking less than 1 second for all 1000 predictions. The KNN is similarly fast with 2.2 seconds. Both methods increase with the number of grid cells as the grid cell size becomes smaller and thus the input features become larger. The Bagged Trees are slower than KNN and Gaussian SVM for a small number of grid cells, but the runtime increases proportionally less as the number of grid cells increases. Consequently,

Table 3: Regression error results as the average absolute error ($\cdot 10^2$) of a 5-fold cross validation, normalized to the image resolution. The columns X and Y denote the position of the bounding box, W is the width, and H is the height of the bounding box. The best values per method are highlighted in bold.

Feat. ML Grid	Time window size (in ms)																					
	100				200				300				400				500					
	X	Y	W	H	X	Y	W	H	X	Y	W	H	X	Y	W	H	X	Y	W	H		
2D heatmap	Gaussian Process	5	7.0	8.0	13.8	16.4	7.2	7.9	13.4	16.1	7.7	8.2	13.9	16.1	7.8	8.0	13.7	16.1	8.8	7.3	13.4	16.3
		10	6.1	6.8	13.0	15.3	6.5	6.9	12.5	15.2	8.8	7.5	13.8	15.3	8.1	7.1	13.2	16.5	8.2	6.9	13.8	15.5
		15	6.1	6.8	12.7	15.3	7.8	9.5	13.5	16.8	9.4	8.4	14.3	15.7	8.3	7.7	12.4	15.8	8.4	7.1	13.7	15.8
		20	6.2	6.9	12.9	15.3	8.8	10.2	14.1	17.0	9.4	9.9	13.7	16.3	8.1	7.6	12.4	15.4	8.5	8.5	13.2	17.5
		25	6.8	6.8	12.7	15.2	8.8	8.8	13.9	16.8	9.3	9.2	14.3	15.9	8.4	8.9	13.0	15.8	8.5	8.5	13.4	17.0
		30	8.6	6.8	12.9	15.4	8.8	10.8	14.0	17.3	9.3	11.1	14.3	17.7	8.7	10.6	14.1	17.3	8.9	8.6	13.7	17.5
		35	7.9	6.8	12.7	15.1	8.8	10.8	13.4	17.3	9.3	11.1	14.3	17.7	8.7	10.6	14.1	17.3	8.6	8.6	13.9	17.5
		40	8.1	6.8	12.2	16.4	9.1	10.8	12.7	17.3	9.3	11.1	14.3	17.7	8.7	10.6	14.1	17.3	8.6	10.3	13.8	17.5
		45	8.1	6.8	12.6	16.9	9.1	10.8	14.2	17.3	9.3	11.1	14.3	17.7	8.7	10.6	14.1	17.3	9.1	10.3	14.4	17.5
		50	8.0	6.8	12.6	16.8	9.1	10.8	14.2	17.3	9.3	11.1	14.3	17.7	8.7	10.6	14.1	17.3	9.1	10.3	14.4	17.5
2D heatmap	Bagged Trees	5	7.0	7.9	13.5	16.4	7.2	7.7	13.2	16.3	7.6	8.1	13.4	16.1	7.4	7.8	13.5	15.7	7.8	7.3	13.6	15.7
		10	6.4	7.0	13.0	15.3	6.7	7.1	12.6	15.2	7.4	7.9	12.5	15.3	7.0	7.7	12.5	14.9	7.4	7.3	12.5	15.0
		15	6.4	7.1	12.6	15.1	6.8	7.3	12.3	14.9	7.5	8.0	12.5	15.3	7.2	7.9	12.0	15.0	7.8	7.2	12.2	15.1
		20	6.4	6.9	12.7	14.8	6.9	7.1	12.2	14.8	7.6	8.0	12.2	15.4	7.1	7.8	12.2	15.0	7.7	7.2	12.1	14.9
		25	6.5	7.0	12.6	14.8	7.1	7.4	12.2	14.7	7.7	8.2	12.1	14.8	7.2	7.9	12.1	14.6	7.7	7.4	12.0	14.7
		30	6.5	6.9	12.4	14.7	6.9	7.3	12.2	14.6	7.6	8.2	12.4	15.0	7.3	7.9	12.2	14.7	7.7	7.4	12.3	15.1
		35	6.4	7.0	12.2	14.5	7.1	7.3	12.1	14.4	7.6	8.2	12.1	14.8	7.3	7.9	12.1	14.4	7.8	7.5	12.1	14.7
		40	6.5	7.0	12.1	14.3	7.1	7.3	12.0	14.4	7.6	8.2	12.0	14.5	7.4	8.0	12.1	14.6	7.8	7.4	12.0	14.4
		45	6.5	7.0	12.2	14.4	7.1	7.4	12.1	14.5	7.6	8.3	12.1	14.8	7.2	8.0	12.0	14.5	7.6	7.6	12.0	14.8
		50	6.6	7.1	12.3	14.4	7.1	7.4	12.2	14.4	7.6	8.3	12.3	14.5	7.3	8.1	12.1	14.6	7.8	7.5	12.0	15.0
2D heatmap	Gaussian SVM	5	7.2	8.3	14.6	17.2	7.4	8.2	14.6	16.8	8.1	8.7	14.6	17.3	7.6	8.3	14.3	16.5	7.7	7.9	14.7	16.8
		10	6.5	7.1	14.5	16.9	6.8	7.0	14.3	16.6	7.5	7.7	14.4	17.2	7.0	7.3	14.0	16.4	7.3	6.9	14.6	16.7
		15	6.4	7.0	14.4	16.6	6.9	7.0	13.9	16.2	7.6	7.8	14.0	16.7	7.1	7.4	13.8	16.0	7.5	7.1	14.2	16.1
		20	6.5	7.0	14.4	16.6	6.9	7.2	14.1	16.4	7.5	7.9	14.2	16.8	7.1	7.3	13.9	16.1	7.6	7.1	14.3	16.3
		25	6.5	6.9	14.0	16.4	7.0	7.2	13.8	16.0	7.6	7.8	13.9	16.5	7.2	7.6	13.8	15.8	7.7	7.2	14.1	15.9
		30	6.5	6.9	14.1	16.4	7.0	7.2	14.0	16.4	7.7	8.1	14.1	16.8	7.3	7.8	13.7	16.0	7.8	7.5	14.1	16.1
		35	6.4	7.0	13.7	16.0	7.0	7.2	13.7	15.8	7.7	8.0	13.7	16.1	7.3	7.8	13.4	15.6	7.7	7.4	13.7	15.7
		40	6.5	7.0	13.7	16.0	7.1	7.5	13.7	15.9	7.8	8.1	13.8	16.2	7.4	7.8	13.5	15.5	7.8	7.7	13.8	15.7
		45	6.6	7.0	13.9	16.3	7.1	7.4	13.8	16.0	7.8	8.3	14.0	16.6	7.5	8.0	13.7	16.0	7.9	7.7	14.1	16.2
		50	6.5	7.0	13.9	16.1	7.1	7.6	13.9	16.0	7.9	8.3	14.1	16.4	7.5	8.1	13.9	15.8	7.9	7.9	14.2	16.0
3D heatmap	Gaussian Process	5	6.7	7.5	12.8	15.4	7.1	7.3	12.4	15.7	9.4	8.6	13.1	16.6	8.6	8.4	13.2	15.6	8.9	7.3	13.8	15.2
		10	5.8	6.2	11.4	12.9	7.6	7.6	12.2	16.8	9.3	11.1	14.3	17.7	8.7	10.6	14.1	17.3	8.9	8.6	12.9	17.5
		15	6.5	6.0	10.4	11.6	9.1	10.8	14.2	17.2	9.3	11.1	14.3	17.7	8.7	10.6	14.1	17.3	9.1	10.3	14.4	17.5
		20	7.4	8.3	9.9	16.3	9.1	10.8	14.2	17.3	9.3	11.1	14.3	17.7	8.7	10.6	14.1	17.3	9.1	10.3	14.4	17.5
		25	9.1	10.8	14.3	17.4	9.1	10.8	14.2	17.3	9.3	11.1	14.3	17.7	8.7	10.6	14.1	17.3	9.1	10.3	14.4	17.5
		30	9.1	10.8	14.3	17.4	9.1	10.8	14.2	17.3	9.3	11.1	14.3	17.7	8.7	10.6	14.1	17.3	9.1	10.3	14.4	17.5
		35	9.1	10.8	14.3	17.4	9.1	10.8	14.2	17.3	9.3	11.1	14.3	17.7	8.7	10.6	14.1	17.3	9.1	10.3	14.4	17.5
		40	9.1	10.8	14.3	17.4	9.1	10.8	14.2	17.3	9.3	11.1	14.3	17.7	8.7	10.6	14.1	17.3	9.1	10.3	14.4	17.5
		45	9.1	10.8	14.3	17.4	9.1	10.8	14.2	17.3	9.3	11.1	14.3	17.7	8.7	10.6	14.1	17.3	9.1	10.3	14.4	17.5
		50	9.1	10.8	14.3	17.4	9.1	10.8	14.2	17.3	9.3	11.1	14.3	17.7	8.7	10.6	14.1	17.3	9.1	10.3	14.4	17.5
3D heatmap	Bagged Trees	5	6.7	7.4	12.7	15.2	7.1	7.5	12.3	15.0	7.9	7.9	12.5	15.2	7.6	7.7	12.5	15.0	7.8	7.5	12.6	15.2
		10	6.4	6.7	11.8	13.8	7.0	7.2	11.5	14.0	7.6	8.1	11.9	14.7	7.3	8.2	11.6	14.1	7.7	7.8	11.4	14.3
		15	6.4	6.8	11.1	12.8	7.1	7.3	11.0	13.0	7.8	8.3	11.4	13.6	7.3	8.3	11.6	13.3	8.2	7.7	11.1	13.4
		20	6.7	7.0	11.0	12.7	7.2	7.3	11.0	13.1	7.9	8.2	11.1	13.4	7.5	8.2	11.2	13.5	8.1	7.8	10.9	13.6
		25	6.6	7.1	10.9	12.6	7.2	7.6	11.0	12.6	7.8	8.6	10.9	13.2	7.5	8.4	11.1	13.1	8.2	7.9	10.5	12.8
		30	6.8	7.2	10.8	12.3	7.5	7.8	11.0	12.7	8.1	8.6	10.9	13.4	7.8	8.7	11.1	13.3	8.4	8.2	10.8	12.9
		35	7.0	7.3	11.0	13.0	7.4	7.8	11.2	13.1	8.1	8.7	11.0	13.8	7.7	8.6	11.0	13.8	8.3	8.2	10.8	13.3
		40	7.1	7.5	10.7	12.6	7.5	8.0	10.9	12.8	8.1	8.8	11.0	13.5	7.7	8.8	10.6	13.4	8.5	8.3	10.5	13.3
		45	7.2	7.6	10.7	12.6	7.6	7.9	11.0	13.1	8.3	8.8	11.1	13.7	7.8	8.9	11.0	13.4	8.5	8.5	10.9	13.3
		50	7.2	7.7	10.9	12.9	7.6	8.1	11.1	13.2	8.2	9.0	11.0	13.6	7.8	9.0	11.0	13.5	8.3	8.7	10.9	13.9
3D heatmap	Gaussian SVM	5	7.1	7.9	14.0	16.9	7.3	7.8	13.9	16.7	8.0	8.3	13.7	17.1	7.6	8.1	13.4	16.4	8.0	7.6	13.2	16.3
		10	6.4	6.8	13.3	15.8	6.9	6.9	13.3	15.7	7.4	7.7	12.9	15.7	7.3	7.9	12.9	15.4	7.5	7.5	12.9	15.3
		15	6.2	6.5	12.4	14.1	7.0	6.8	12.6	14.4	7.5	7.8	12.7	15.0	7.3	8.0	12.8	14.7	7.7	7.8	13.0	14.8
		20	6.2	6.3	11.9	13.9	6.9	7.0	12.0	14.1	7.5	8.1	12.5	15.0	7.6	8.1	12.5	14.7	7.8	8.1	13.0	14.8
		25	6.3	6.2	11.5	13.5	6.9	7.2	11.8	13.8	7.7	8.4	12.3	14.8	7.5	8.4	12.4	14.4	8.0	8.3	13.0	15.0
		30	6.3	6.3	11.1	13.0	7.1	7.5	11.8	13.9	7.9	8.6	12.4	15.0	7.6	8.6	12.4	14.6	8.2	8.5	13.0	15.0
		35	6.4	6.2	11.2	13.0	7.3	7.5	11.8	13.9	8.1	8.7	12.4	15.1	7.7	8.6	12.4	14.8	8.2	8.6	13.2	15.5
		40	6.5	6.3	11.0	12.9	7.4	7.7	11.9	14.0	8.1	8.8	12.5	15.2	7.8	8.7	12.4	14.8	8.3	8.7	13.3	15.4
		45	6.6	6.6	11.3	13.1	7.5	7.8	12.1	14.1	8.3	8.9	12.6	15.3	7.9	8.8	12.7	15.0	8.4	8.8	13.5	15.7
		50	6.6	6.7	11.2	13.0	7.5	8.0	12.2	14.3	8.4	9.1	12.8	15.5	7.9	9.0	12.8	15.2	8.4	8.9	13.7	15.8

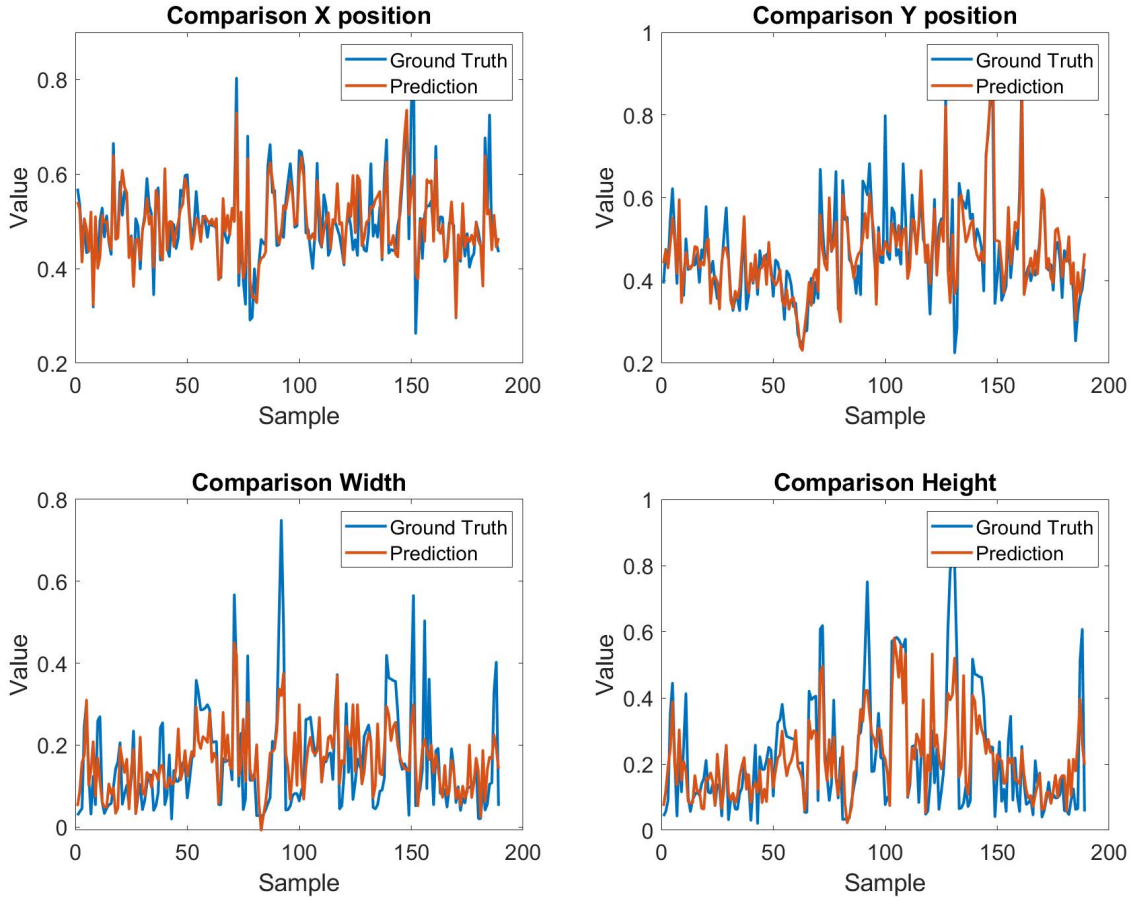


Figure 4: Qualitative evaluation of the bounding box parameter regression. Ground truth in blue and the prediction in red. The y-axis represents the value and the x-axis the sample number. The results are from the Gaussian Process Regression with a time window size of 100, a grid cell number of 15 and the 3D heatmap feature.

even with large input sizes, the runtime for the 3D heatmap feature is in the range of one minute for the 1000 predictions while the runtime for KNN and Gaussian SVM increases considerably from a few seconds to several minutes. Nonetheless, it is immediately apparent that the runtime is in general significantly lower compared to the object detectors using the RGB images as input features. While only the smaller models like YOLOv5n and SSDlite remain under three minutes, the other models are much slower. In particular, the computation time required by the popular Faster R-CNN with a ResNet-50 backbone exceeds that of the Bagged Trees by a factor of over 100, even with the largest 3D heatmap input feature.

A similar picture emerges with respect to the RAM allocated for one single prediction. The memory requirements of the bagged trees are larger at the beginning, but do not increase as much in proportion to the number of grid cells as for the KNN and the Gaussian SVM. These even require less than 1 MB of memory for small inputs and to some extent only a few 100 KB. The demand by the bagged trees is in the range of only one and two megabytes for all grid sizes. Even in the case with the narrowest grid pattern. Here, KNN and Gaussian SVM require over 12 MB and 15 MB, respectively. However, this is substantially less than the most frugal neural network YOLOv5n, which needs around 270 MB. Faster R-CNN with the ResNet-50 backbone requires the most memory with over 1.7 GB. Again, the factor is more than 100 times larger than for the Gaussian SVM with the maximum number of grid cells. Compared to the Bagged Trees, it even exceeds 860 times.

In summary, our method is several orders of magnitude faster than conventional object detectors while requiring only a fraction of their resources.

Table 4: Comparison of the required resources for the different input features. The time column indicates the execution time for 1000 different inputs at a batch size of one in seconds. The memory column specifies the required memory of a single input in kilobytes. For the 2D and 3D heatmap features, a time window size of 250 ms was used.

Feature	ML	Time [s]					Memory [KB]				
		Grid cells					Grid cells				
		10	20	30	40	50	10	20	30	40	50
2D heatmap	KNN	2.2	4.8	10.8	18.4	27.0	116	259	424	607	810
	Bagged Trees	52.1	56.6	57.8	58.9	60.0	954	1106	1134	1147	1164
	Gaussian SVM	0.9	2.9	8.6	19.3	37.7	108	238	406	584	840
3D heatmap		Grid cells					Grid cells				
		10	20	30	40	50	10	20	30	40	50
	KNN	12.0	80.9	276.9	620.5	1137.2	328	1214	3045	6278	12769
	Bagged Trees	58.1	61.9	64.7	66.9	74.2	1226	1318	1467	1699	2020
	Gaussian SVM	11.9	154.9	610.6	1811.1	4061.6	325	1360	3650	7443	15368
RGB Image	Faster R-CNN [27] (RN50)	8 705.3				1 745 456					
	Faster R-CNN [27] (MN)	1 205.6				545 400					
	FCOS [32]	4 723.2				995 416					
	RetinaNet [17]	5 184.5				1 390 580					
	SSD300 [19]	900.8				529 744					
	SSDlite320 [19]	163.7				293 788					
	YOLOv5n [13]	200.6				270 168					
	YOLOv5s [13]	486.3				312 104					
	YOLOv5m [13]	1 127.6				421 904					
YOLOv5l [13]	2 174.5				622 536						
YOLOv5x [13]	3 677.9				940 508						

5 Limitations

We have shown that the gaze data can be used to detect objects and their bounding boxes. What is still missing for an actual application is the combinatorial use with, e.g., a robot, which learns to detect these objects. This application, of course, still brings some challenges like inaccurate bounding boxes or wrongly detected objects. However, with a robot or a machine learning the objects, there are more possibilities like depth data and the image information from different perspectives. Thus, there are also more possibilities for optimization in this application. Another limitation of our work is that we did not perform a parameter search for the machine learning methods. This means that our results are certainly far below the possible detection rates that can be achieved. However, our results are easy to reproduce and might be considered rather as a proof-of-concept, yet conveying the potential of gaze in such tasks.

6 Conclusion

In this work, we addressed object detection based on gaze data as well as the regression of the bounding box parameters for the detected objects. Based on evaluations with different parameters of the size of the time window and the grid size of the heatmap feature, our results show that it is possible to detect objects and determine their bounding box based solely on gaze information. This problem is not trivial since the subjects move, and thus, the parameters of the bounding box vary in the time window itself. Additionally, we have used a variety of machine learning methods to show that they work for solving such challenges. Besides, the functionality of several machine learning methods proves that our heatmap feature, which we have extended to 3D, can be used efficiently for this problem. In comparison to classical object detectors that use image input features, we have shown that object detection by means of our heatmap features is significantly faster while only requiring a fraction of the computational resources. This is of major relevance due to the fact that robots usually have only

limited computing capacity at their disposal and cannot be equipped with powerful graphics units as they consume a lot of power.

However, a significant amount of work remains for the future as we plan to extend our proof of concept to a real robot by making the gaze of the human collaborator accessible to it. Our approach can serve as a foundation for future applications in the field of human-machine interaction and collaboration, where robots can learn new objects from humans through instant knowledge sharing. Hence, we hope that our methods and our dataset can help to advance researchers in this challenging context.

References

- [1] Jiatong Bao, Yunyi Jia, Yu Cheng, and Ning Xi. Saliency-guided detection of unknown objects in rgb-d indoor scenes. *Sensors*, 15(9):21054–21074, 2015.
- [2] Christian Braunagel, David Geisler, Wolfgang Stolzmann, Wolfgang Rosenstiel, and Enkelejda Kasneci. On the necessity of adaptive eye movement classification in conditionally automated driving scenarios. In *Proceedings of the Ninth Biennial ACM Symposium on Eye Tracking Research & Applications*, pages 19–26, 2016.
- [3] Ravi Teja Chadalavada, Henrik Andreasson, Maike Schindler, Rainer Palm, and Achim J Lilienthal. Bi-directional navigation intent communication using spatial augmented reality and eye-tracking glasses for improved safety in human-robot interaction. *Robotics and Computer-Integrated Manufacturing*, 61:101830, 2020.
- [4] DarkLabel. <https://github.com/darkpgmr/DarkLabel>, 2021. Accessed: 2021-12-07.
- [5] Jia Deng, Wei Dong, Richard Socher, Li-Jia Li, Kai Li, and Li Fei-Fei. Imagenet: A large-scale hierarchical image database. In *Proceedings of the IEEE Conference on Computer Vision and Pattern Recognition (CVPR)*, pages 248–255. IEEE, 2009.
- [6] Wolfgang Fuhl, Nikolai Sanamrad, and Enkelejda Kasneci. The gaze and mouse signal as additional source for user fingerprints in browser applications. *arXiv preprint arXiv:2101.03793*, 2021.
- [7] Wolfgang Fuhl, Daniel Weber, and Enkelejda Kasneci. Pistol: Pupil invisible supportive tool to extract pupil, iris, eye opening, eye movements, pupil and iris gaze vector, and 2d as well as 3d gaze. *arXiv preprint arXiv:2201.06799*, 01 2022.
- [8] Alyona I Grushko and Sergey V Leonov. The usage of eye-tracking technologies in rock-climbing. *Procedia-Social and Behavioral Sciences*, 146:169–174, 2014.
- [9] Katarzyna Harezlak and Pawel Kasprowski. Application of eye tracking in medicine: A survey, research issues and challenges. *Computerized Medical Imaging and Graphics*, 65:176–190, 2018.
- [10] Kaiming He, Xiangyu Zhang, Shaoqing Ren, and Jian Sun. Deep residual learning for image recognition. In *Proceedings of the IEEE conference on computer vision and pattern recognition*, pages 770–778, 2016.
- [11] Benedikt W Hosp, Florian Schultz, Oliver Höner, and Enkelejda Kasneci. Soccer goalkeeper expertise identification based on eye movements. *PloS one*, 16(5):e0251070, 2021.
- [12] Andrew Howard, Mark Sandler, Grace Chu, Liang-Chieh Chen, Bo Chen, Mingxing Tan, Weijun Wang, Yukun Zhu, Ruoming Pang, Vijay Vasudevan, et al. Searching for mobilenetv3. In *Proceedings of the IEEE/CVF international conference on computer vision*, pages 1314–1324, 2019.
- [13] Glenn Jocher, Ayush Chaurasia, Alex Stoken, Jirka Borovec, NanoCode012, Yonghye Kwon, TaoXie, Jiacong Fang, imyhxy, Kalen Michael, Lorna, Abhiram V, Diego Montes, Jébastien Nadar, Laughing, tkianai, yxNONG, Piotr Skalski, Zhiqiang Wang, Adam Hogan, Cristi Fati, Lorenzo Mammana, AlexWang1900, Deep Patel, Ding Yiwei, Felix You, Jan Hajek, Laurentiu Diaconu, and Mai Thanh Minh. ultralytics/yolov5: v6.1 - TensorRT, TensorFlow Edge TPU and OpenVINO Export and Inference, February 2022.

- [14] Ben Kehoe, Akihiro Matsukawa, Sal Candido, James Kuffner, and Ken Goldberg. Cloud-based robot grasping with the google object recognition engine. In *2013 IEEE International Conference on Robotics and Automation*, pages 4263–4270. IEEE, 2013.
- [15] Gert Kootstra, Niklas Bergström, and Danica Kragic. Fast and automatic detection and segmentation of unknown objects. In *2010 10th IEEE-RAS International Conference on Humanoid Robots*, pages 442–447. IEEE, 2010.
- [16] Yin Li, Xiaodi Hou, Christof Koch, James M Rehg, and Alan L Yuille. The secrets of salient object segmentation. In *Proceedings of the IEEE conference on computer vision and pattern recognition*, pages 280–287, 2014.
- [17] Tsung-Yi Lin, Priya Goyal, Ross Girshick, Kaiming He, and Piotr Dollár. Focal loss for dense object detection. In *Proceedings of the IEEE international conference on computer vision*, pages 2980–2988, 2017.
- [18] Tsung-Yi Lin, Michael Maire, Serge Belongie, James Hays, Pietro Perona, Deva Ramanan, Piotr Dollár, and C Lawrence Zitnick. Microsoft COCO: Common objects in context. In *European conference on computer vision*, pages 740–755. Springer, 2014.
- [19] Wei Liu, Dragomir Anguelov, Dumitru Erhan, Christian Szegedy, Scott Reed, Cheng-Yang Fu, and Alexander C Berg. Ssd: Single shot multibox detector. In *European conference on computer vision*, pages 21–37. Springer, 2016.
- [20] Xiaoxue Luo, Junjie Shen, Hong Zeng, Aiguo Song, Baoguo Xu, Huijun Li, Pengcheng Wen, and Cong Hu. Interested object detection based on gaze using low-cost remote eye tracker. In *2019 9th International IEEE/EMBS Conference on Neural Engineering (NER)*, pages 1101–1104. IEEE, 2019.
- [21] Jeffrey Mahler, Matthew Matl, Vishal Satish, Michael Danielczuk, Bill DeRose, Stephen McKinley, and Ken Goldberg. Learning ambidextrous robot grasping policies. *Science Robotics*, 4(26), 2019.
- [22] Oskar Palinko, Andrew L Kun, Alexander Shyrovkov, and Peter Heeman. Estimating cognitive load using remote eye tracking in a driving simulator. In *Proceedings of the 2010 symposium on eye-tracking research & applications*, pages 141–144, 2010.
- [23] Oskar Palinko, Francesco Rea, Giulio Sandini, and Alessandra Sciutti. Robot reading human gaze: Why eye tracking is better than head tracking for human-robot collaboration. In *2016 IEEE/RSJ International Conference on Intelligent Robots and Systems (IROS)*, pages 5048–5054. IEEE, 2016.
- [24] Derek Panchuk, Samuel Vine, and Joan N Vickers. Eye tracking methods in sport expertise. In *Routledge handbook of sport expertise*, pages 176–187. Routledge, 2015.
- [25] Youwei Pang, Xiaoqi Zhao, Lihe Zhang, and Huchuan Lu. Multi-scale interactive network for salient object detection. In *Proceedings of the IEEE/CVF Conference on Computer Vision and Pattern Recognition*, pages 9413–9422, 2020.
- [26] Pupil Labs. <https://pupil-labs.com/>, 2021. Accessed: 2021-12-07.
- [27] Shaoqing Ren, Kaiming He, Ross Girshick, and Jian Sun. Faster R-CNN: Towards real-time object detection with region proposal networks. *Advances in Neural Information Processing Systems*, 28:91–99, 2015.
- [28] Mark Sandler, Andrew Howard, Menglong Zhu, Andrey Zhmoginov, and Liang-Chieh Chen. Mobilenetv2: Inverted residuals and linear bottlenecks. In *Proceedings of the IEEE conference on computer vision and pattern recognition*, pages 4510–4520, 2018.
- [29] Karthikeyan Shanmuga Vadivel, Thuyen Ngo, Miguel Eckstein, and BS Manjunath. Eye tracking assisted extraction of attentionally important objects from videos. In *Proceedings of the IEEE Conference on Computer Vision and Pattern Recognition*, pages 3241–3250, 2015.
- [30] Ran Shi, Ngi King Ngan, and Hongliang Li. Gaze-based object segmentation. *IEEE Signal Processing Letters*, 24(10):1493–1497, 2017.

- [31] Karen Simonyan and Andrew Zisserman. Very deep convolutional networks for large-scale image recognition. *arXiv preprint arXiv:1409.1556*, 2014.
- [32] Zhi Tian, Chunhua Shen, Hao Chen, and Tong He. FCOS: Fully convolutional one-stage object detection. In *The IEEE International Conference on Computer Vision (ICCV)*, 2019.
- [33] Geoffrey Tien, M Stella Atkins, Bin Zheng, and Colin Swindells. Measuring situation awareness of surgeons in laparoscopic training. In *Proceedings of the 2010 symposium on eye-tracking research & applications*, pages 149–152, 2010.
- [34] Takumi Toyama, Thomas Kieninger, Faisal Shafait, and Andreas Dengel. Gaze guided object recognition using a head-mounted eye tracker. In *Proceedings of the 2012 ACM Symposium on Eye Tracking Research & Applications*, pages 91–98. ACM, 2012.
- [35] A Van der Gijp, CJ Ravesloot, H Jarodzka, MF Van der Schaaf, IC Van der Schaaf, Jan PJ van Schaik, and Th J Ten Cate. How visual search relates to visual diagnostic performance: a narrative systematic review of eye-tracking research in radiology. *Advances in Health Sciences Education*, 22(3):765–787, 2017.
- [36] Daniel Weber, Enkelejda Kasneci, and Andreas Zell. Exploiting augmented reality for extrinsic robot calibration and eye-based human-robot collaboration. In *Proceedings of the 2022 ACM/IEEE International Conference on Human-Robot Interaction*, 2022.
- [37] Daniel Weber, Thiago Santini, Andreas Zell, and Enkelejda Kasneci. Distilling location proposals of unknown objects through gaze information for human-robot interaction. In *2020 IEEE/RSJ International Conference on Intelligent Robots and Systems (IROS)*, pages 11086–11093. IEEE, 2020.
- [38] Fen Xiao, Liangchan Peng, Lei Fu, and Xieping Gao. Salient object detection based on eye tracking data. *Signal Processing*, 144:392–397, 2018.
- [39] Junli Xu, Jianliang Min, and Jianfeng Hu. Real-time eye tracking for the assessment of driver fatigue. *Healthcare technology letters*, 5(2):54–58, 2018.
- [40] Kiwon Yun, Yifan Peng, Dimitris Samaras, Gregory J Zelinsky, and Tamara L Berg. Exploring the role of gaze behavior and object detection in scene understanding. *Frontiers in psychology*, 4:917, 2013.